Dalton Transactions

ROYAL SOCIETY OF CHEMISTRY

PAPER

View Article Online
View Journal

Cite this: DOI: 10.1039/d0dt03500a

Iron(III)-bipyridine incorporated metal–organic frameworks for photocatalytic reduction of CO_2 with improved performance†

Yuan-Ping Wei,‡[a] Sizhuo Yang,‡[b] Peng Wang,[a] Jin-Han Guo,[a] Jier Huang *[b] and Wei-Yin Sun *[a]

Received 9th October 2020,
Accepted 30th November 2020

DOI: 10.1039/d0dt03500a

rsc.li/dalton

Metal–organic frameworks (MOFs) represent an emerging class of platforms to assemble single site photocatalysts for artificial photosynthesis. In this work, we report a new CO_2 reduction photocatalyst (UiO-68-Fe-bpy) based on a robust Zr(IV)-MOF platform with incorporated Fe(bpy)Cl_3 (bpy refers to the 4′-methyl-[2,2′-bipyridine] moiety) *via* amine–aldehyde condensation. We show that this hybrid catalyst can reduce CO_2 to form CO under visible light illumination with excellent selectivity and enhanced activity with respect to its parent MOF and corresponding homogeneous counterpart. Using steady state and transient absorption (TA) spectroscopy, we show that the enhanced photocatalytic activity of UiO-68-Fe-bpy is attributed to the elongated excited state lifetime of Fe(bpy)Cl_3 after being incorporated to the UiO-68-NH_2 platform. This work demonstrates the great potential of MOFs as a next generation platform for solar fuel conversion.

Introduction

With soared energy demand and intensified global warming, the search for effective conversion of CO_2 into valuable chemicals is an important but challenging task.[1–3] Inspired by nature, chemists express strong interest in the systems that can photocatalytically reduce CO_2 to energy carrier products such as CH_4, CH_3OH, HCOOH and CO.[4] These systems include homogeneous transition-metal complexes,[5] heterogeneous metal-incorporated zeolites,[6] and inorganic semiconductors.[7–12] However, the homogeneous transition-metal complexes are often not recyclable although many of them show high efficiency in reducing CO_2 in the presence of photosensitizers.[13] On the other hand, the metal-incorporated zeolites and inorganic semiconductors are robust but often suffer poor efficiency for the photocatalytic reduction of CO_2.[14] Therefore, developing new photocatalysts with high efficiency and stability is necessary in order to convert CO_2 to useful chemical fuels.

Metal–organic frameworks (MOFs), constructed from metal ion or metal cluster nodes interconnected with organic ligands, are a class of crystalline micro-/meso-porous materials and have been explored for a variety of potential applications including drug delivery,[15,16] gas storage,[17–19] chemical separation and catalysis.[20–26] In particular, MOFs have shown great potential for photocatalytic CO_2 reduction by incorporating catalytic sites into a porous and robust MOF matrix.[27–37] Among the systems reported, one valuable strategy is to incorporate organometallic species into MOFs by post-synthetic modification (PSM), where the organometallic species serve as both a photosensitizer and a CO_2-reduction catalyst such that the photocatalytic system can take advantage of both homogenous and heterogeneous catalysts.[38–42] For example, molecular complexes based on noble metals such as platinum, ruthenium and iridium have been incorporated into MOFs, which demonstrate catalytic activity for photocatalytic CO_2 reduction.[43–45] Molecular complexes based on cost effective and earth abundant transition metals including iron, cobalt, manganese and nickel have also been reported in recent years.[46–48] While these examples demonstrate the great potential of MOFs as single site photocatalysts for CO_2 reduction, the selectivity and efficiency of most of these systems need to be improved.

Among the reported MOFs, UiO-series (UiO = University of Oslo) have high thermal and chemical stability, which are

[a]*Coordination Chemistry Institute, State Key Laboratory of Coordination Chemistry, School of Chemistry and Chemical Engineering, Nanjing National Laboratory of Microstructures, Collaborative Innovation Center of Advanced Microstructures, Nanjing University, Nanjing 210023, China. E-mail: sunwy@nju.edu.cn*
[b]*Department of Chemistry, Marquette University, Milwaukee, Wisconsin 53201, USA. E-mail: jier.huang@marquette.edu*

†Electronic supplementary information (ESI) available: Synthesis and characterization of UiO-68-NH_2 and UiO-68-Fe-bpy, photocatalytic experiments, UV-Vis, MS, IR, ^{1}HNMR, XPS, TGA, EXAFS, femtosecond TA spectra, XRPD patterns, SEM images and gas adsorption experiments. See DOI: 10.1039/d0dt03500a

‡These authors contributed equally.

essential requirements of photocatalysts. The reports on modified UiO-68 for photoreduction are far fewer than those on UiO-66 and UiO-67.[49,50] However, the larger cavity and better CO_2 adsorbability imply that UiO-68 could be the ideal platform for the photoreduction of CO_2. On the other hand, iron complexes have been shown to be efficient molecular catalysts for CO_2-to-CO conversion.[51] Besides, the redox active 2,2′-bipyridine ligand can serve as an electron reservoir and is expected to promote proton-coupled electron transfer (PCET) reactions by combining with iron.[52] Therefore, it is meaningful that the Fe-bpy complex and UiO-68 MOF are selected to assemble an efficient photocatalyst for CO_2 reduction.

Herein, we report a new MOF-based single site photocatalyst, *i.e.* UiO-68-Fe-bpy (bpy refers to 4′-methyl-[2,2′-bipyridine] moiety), synthesized based on UiO-68-NH_2 and 4′-methyl-[2,2′-bipyridine]-4-carbaldehyde (bpy-CHO) using an amine–aldehyde condensation and post-synthetic chelated metalation with $FeCl_3$ (Scheme 1). Under visible light illumination, we show that UiO-68-Fe-bpy can reduce CO_2 to form CO with excellent selectivity and demonstrate much better performance than its homogeneous counterpart with the same Fe(bpy)Cl_3 moiety. The enhanced photocatalytic performance of UiO-68-Fe-bpy can be attributed to the prolonged excited state lifetime of the Fe(bpy)Cl_3 moiety in UiO-68-Fe-bpy as confirmed by femtosecond transient absorption (TA) spectroscopy.

Experimental

Synthesis of UiO-68-Fe-bpy

The as-synthesized UiO-68-NH_2 (0.03 mmol, 0.08 g) was suspended in MeOH (5 mL) under ultrasound conditions, and then bpy-CHO (0.81 mmol, 0.16 g) was dissolved in MeOH (5 mL) followed by the addition of acetic acid (HOAc) (25 μL). The mixture was refluxed at 70 °C for 24 h. Afterwards, the precipitate was collected by centrifugation and washed with abundant MeOH (three times) and dried in air. The new MOF particles were dispersed in MeOH (10 mL), and then $FeCl_3$ (1.54 mmol, 0.25 g) was added, and the mixture was heated at 70 °C for an additional 12 h. The resulting precipitate was collected by centrifugation and washed with abundant MeOH (three times) and dried in a vacuum. IR (KBr pellet, cm^{-1}) 3429 (m), 1700 (m), 1600 (vs), 1533 (m), 1420 (s), 1182 (w), 1104 (w), 785 (m), 713 (w), 657 (m), 567 (w), 467 (w).

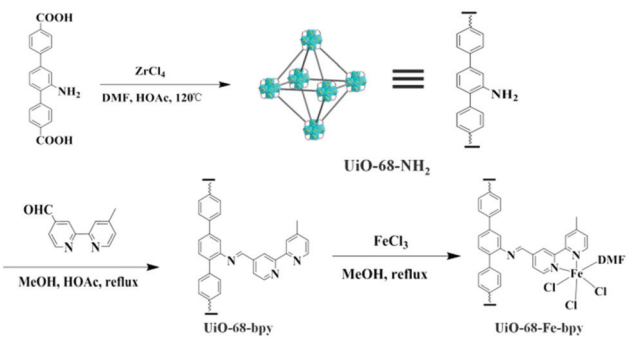

Scheme 1 Synthesis of UiO-68-Fe-bpy.

Photochemical CO_2 reduction experiments

The photocatalytic activities of all samples were carried out in a batch-type reaction system (CEL-SPH2N-D9, CeAulight, China) equipped with a homemade photoreactor and a homemade circulating water filter to avoid the photothermal effect. 2 mg of sample was dispersed in 1 mL of acetone and ultrasonicated for 5 minutes, and then the suspension was uniformly dispersed onto a glass fiber film (Φ 25 mm, 0.22 μm pore diameter) drop by drop under an infrared lamp. The film was activated in a vacuum at 120 °C for 12 h. Then the film was placed in the reaction cell, and 2 mL of triethanolamine (TEOA) was added into the reactor, and the reactor was maintained at 50 °C using an oil bath. After complete evacuation of the reaction system (no O_2 or N_2 could be detected), 80 kPa of pure CO_2 gas (99.999%, Tianhong Gas) was injected into the airtight system. A 300 W xenon arc lamp (Sirius-300P, Zolix Instruments Co., Ltd, China) with a 400–780 nm filter (CeAulight, China) was used as the light source. The optical power density was set at 200 mW cm^{-2}, which was measured using an optical power meter (CEL-NP2000-2, CeAulight, China). The gas products were monitored using gas chromatography (GC-9860, Luchuang Instrument, China), equipped with a TCD to measure H_2, and an FID detector with a methane conversion oven to convert CO and CO_2 into CH_4 before entering the FID. The gas was separated by a 1 m TDX-01 column with N_2 (99.999%) as the carrier gas, and the temperatures for the TCD, FID, column and methane converter were 100, 150, 100 and 360 °C, respectively. The retention times of CO, CH_4 and H_2 were 1.290, 2.540 and 0.578 min, respectively. The calibration curves for gases were established separately.

Femtosecond transient absorption (TA) spectroscopy

The Femtosecond TA setup is based on a regenerative amplified Ti-Sapphire laser system (Solstice, 800 nm, <100 fs FWHM, 3.5 mJ per pulse, 1 kHz repetition rate). The tunable (235–1100 nm) pump was generated by TOPAS from seventy-five percent of the Solstice output and was chopped at 500 Hz. The remaining twenty-five percent of the Solstice output was used to generate white light in a sapphire crystal (420–800 nm) in a Helios ultrafast spectrometer (Ultrafast Systems LLC). To make thin films for TA measurements, 1 mg of sample was added into 0.5 mL of Nafion (5% w/w in water and 1-propanol) in a glass vial. The hybrid was stirred for 2 h and then distributed uniformly on a piranha-etched glass. The samples were dried in air. The film samples were constantly translated in the case of heating and permanent degradation. The pump power at 440 nm is 0.2 mW for all measurements.

Results and discussion

Synthesis of UiO-68-Fe-bpy

Briefly, the yellowish crystalline UiO-68-NH_2 was obtained by a solvothermal reaction of amino-triphenyldicarboxylic acid (NH_2-TPDC) and $ZrCl_4$ in DMF in the presence of HOAc as a modulator.[53,54] UiO-68-NH_2 was then treated with bpy-CHO (excess) and HOAc in MeOH at 70 °C for 24 h to afford UiO-68-bpy *via* an amine–aldehyde condensation. UiO-68-Fe-bpy was achieved by metalation of UiO-68-bpy using $FeCl_3$ (Scheme 1).

The powder X-ray diffraction (PXRD) patterns of the as-synthesized UiO-68-NH_2 and post-modified UiO-68-Fe-bpy agree well with the simulated pattern of UiO-68-NH_2 (Fig. 1a), implying that the crystallinity of UiO-68-NH_2 is retained during the PSM reaction. The SEM images show that UiO-68-NH_2 particles are discrete octahedral crystals with dimensions of 2 to 3 μm per side (Fig. 1b). The post-modified UiO-68-Fe-bpy shows a similar morphology to its parent MOF (Fig. 1c), which further supports that UiO-68-NH_2 is chemically stable during the PSM. The inductively coupled plasma (ICP) measurement of the Zr : Fe ratio of the digested UiO-68-Fe-bpy is 1 : 0.59 (calcd 1 : 1), where the functionalization yield is 59%, which is reasonable as reported previously.[54] We tried by varying the reactant ratio, reaction temperature and time to improve the functionalization yield, and finally got the highest yield of 59%. The limited modification yield may be ascribed to the heterogeneous PSM reaction.

The FT-IR spectra of UiO-68-NH_2 and UiO-68-Fe-bpy in the range of 4000–400 cm^{-1} shown in Fig. S1, ESI† demonstrate the formation of a covalently modified compound. The FT-IR spectrum of UiO-68-NH_2 shows bands at 830 and 1580 cm^{-1} corresponding to the primary amino in- and out-of-plane bending vibrations, respectively.[55] After the amine–aldehyde condensation, the intensity of these characteristic amino peaks decreases. In contrast, the intensity of the peak at 1610 cm^{-1} associated with the N=C stretching vibration increases.[56] These changes imply that UiO-68-NH_2 was successfully modified by amine–aldehyde condensation to generate UiO-68-bpy. In addition, ^1H NMR spectral measurements in DMSO-d_6 for digested UiO-68-NH_2 (Fig. S2a, ESI†) and UiO-68-bpy (Fig. S2b, ESI†) with aqueous HF were performed. The average integration ratio of the signals that originated from bpy-CHO and NH_2-TPDC as observed for the digested UiO-68-bpy sample (Fig. S2b, ESI†) is 0.62, implying that the functionalization yield of bpy-CHO is 62% agreeing with the ICP result of the Fe–Zr ratio, which further confirms the successful combination of bpy-CHO with UiO-68-NH_2. Thermogravimetric analysis (TGA) was performed to examine the thermal stability of the frameworks. The TG curves of UiO-68-NH_2 and UiO-68-Fe-bpy show that they have similar thermal stability (Fig. S3, ESI†).

In addition to the bulk structure, the local geometry of the Fe center was examined by steady-state X-ray absorption spectra (XAS). The control sample was TPDC-Fe-bpy synthesized by the reaction of dimethyl ester of amino-triphenyldicarboxylic acid (amino-TPDC), bpy-CHO and $FeCl_3$ using the method for the preparation of UiO-68-Fe-bpy (Fig. S4, ESI†). Fig. 2a shows the XANES (X-ray absorption near edge structure) spectra of UiO-68-Fe-bpy and TPDC-Fe-bpy measured at the Fe edge. The XANES spectrum of the reference sample ($FeCl_3$ with octahedral geometry) is also shown in Fig. 2a. The main feature observed at 7121.13 eV is assigned to the dipole allowed 1s–4p transition. Additionally, the spectrum of $FeCl_3$ exhibits a sharp pre-edge feature corresponding to the quadrupole allowed 1s–3d transition and is forbidden for a perfect centrosymmetric octahedral geometry, which suggests the distorted octahedral geometry of the Fe center in $FeCl_3$. The XANES spectrum of TPDC-Fe-bpy is similar to that of $FeCl_3$. However, there are some differences between the spectra of UiO-68-Fe-bpy and TPDC-Fe-bpy, including the intensity change of the so called B-feature (dashed line in Fig. 2a), and the different shape and intensity of the absorption peak at region C compared to those of $FeCl_3$ and TPDC-Fe-bpy. These differences were established as a structure sensitive multiple scattering resonance previously,[57,58] implying that the Fe center in the UiO-68-Fe-bpy sample likely adopts a more distorted octahedral geometry. Moreover, the edge energy of both the samples, as shown in the first derivative spectra (the inset of Fig. 2a), is in good agreement with the $FeCl_3$ reference sample, suggesting that the Fe center retains the +3 oxidation state after incorporation.

To gain more insight into the coordination environment, we quantitatively analyzed the extended X-ray absorption fine

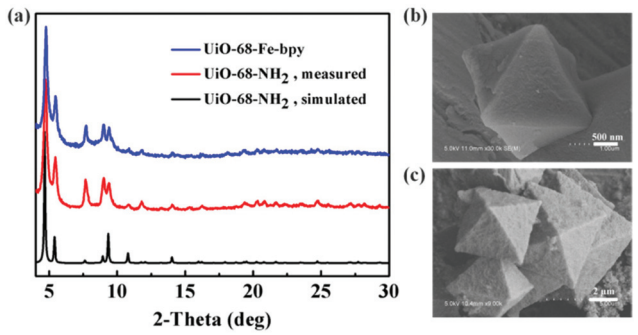

Fig. 1 (a) PXRD patterns of simulated and measured UiO-68-NH_2 and UiO-68-Fe-bpy. SEM images of (b) UiO-68-NH_2 and (c) UiO-68-Fe-bpy.

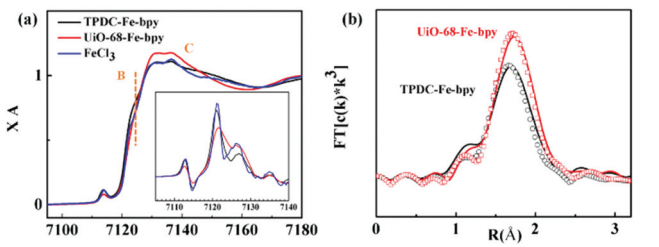

Fig. 2 (a) XANES and (b) Fourier-transform EXAFS spectra of UiO-68-Fe-bpy and TPDC-Fe-bpy at the Fe K-edge. The inset in (a) illustrates the first derivative of the XANES edges. The solid lines and open circles in (b) are experimental and fitted results, respectively.

structure (EXAFS) spectra (Fig. S5, ESI†) using the FeFF model. Fig. 2b shows the EXAFS spectra of UiO-68-Fe-bpy and TPDC-Fe-bpy in R-space. Compared to the spectrum of TPDC-Fe-bpy, the intensity of the peak corresponding to the Fe-ligand first shell (*e.g.* Fe–N and Fe–Cl) in the spectrum of UiO-68-Fe-bpy is reduced, which can be either attributed to the decrease in the Fe coordination number or the increase in disorder. It is unlikely that the coordination number of Fe changes. As a result, the decreased amplitude for the Fe-ligand first shell peak can be attributed to the increased disorder of the Fe coordination environment in UiO-68-Fe-bpy, consistent with the XANES results. In addition, slight reduction of the bond distance of the Fe-ligand first shell in UiO-68-Fe-bpy was observed compared to that of TPDC-Fe-bpy. These results are further supported by the fitting results. The best fitting to the EXAFS experimental data is also shown in Fig. 2b with the fitting parameters being listed in Tables S1 and S2, ESI,† from which we found that the Fe–N distance of UiO-68-Fe-bpy (2.07 Å) is reduced by 0.04 Å compared to that of TPDC-Fe-bpy (2.11 Å). In contrast, while the Fe–Cl distance remains the same (2.18 Å) for both samples, the Debye–Waller factor increases slightly in the UiO-68-Fe-bpy sample with respect to TPDC-Fe-bpy, consistent with the assignment of the increase in disorder. These results together suggest that the coordination geometry for the Fe center in UiO-68-Fe-bpy is largely similar to that of TPDC-Fe-bpy except for the slightly reduced Fe–N distance and increased disorder for Fe–Cl.

X-ray photoelectron spectroscopy (XPS) was employed to explore the elemental composition of UiO-68-Fe-bpy (Fig. S6, ESI†). The peaks at 710.1, 531.6, 400.1, 284.5 and 184.5 eV correspond to the Fe 2p, O 1s, N 1s, C 1s and Zr 3d, respectively. Furthermore, the peak-fitted N 1s core-line spectrum of UiO-68-Fe-bpy (Fig. S7, ESI†) shows the presence of three resolved peaks at 400.4, 399.6 and 398.9 eV, corresponding to the imine (–C═N–), amino (–NH_2) and pyridine N, respectively.[55] Furthermore, the energy dispersive spectroscopy (EDS) spectra (Fig. S8, ESI†) of UiO-68-Fe-bpy disclosed the presence of metal element and the elemental mapping indicates that Fe was modified uniformly throughout the MOF. The atomic ratio of Zr and Fe from EDS is estimated to be 1 : 0.51, which is close to the ICP result.

The gas adsorption properties of the guest-free UiO-68-NH_2 and UiO-68-Fe-bpy were examined to ensure the architectural stability and porosity after PSM. N_2 and CO_2 adsorption isotherms are shown in Fig. S9–S13, ESI.† As expected, the results indicate a decrease in porosity after PSM (Fig. S13, ESI†) with Brunauer–Emmett–Teller (BET) surface areas of 2589.7 and 1372.1 $m^2\ g^{-1}$ for UiO-68-NH_2 (Fig. S9, ESI†) and UiO-68-Fe-bpy (Fig. S10, ESI†), respectively, which can be attributed to the introduction of an Fe(bpy)Cl_3 moiety to the functional ligand of UiO-68-NH_2.[59]

With the PSM of the Fe(bpy)Cl_3 moiety into UiO-68-NH_2, it is expected that UiO-68-Fe-bpy can improve the absorption capacity of visible light compared to UiO-68-NH_2 since the absorption region of TPDC-Fe-bpy extends to 750 nm, which means that TPDC-Fe-bpy (*ca.* 1.69 eV) has a great capacity to absorb visible light (Fig. S14, ESI†). Indeed, the color change from yellow to dark red after metalation was observed due to the coordination of Fe(III) with N atoms of bpy and the presence of ligand-to-metal (bpy→Fe^{III}) charge transfer (LMCT), from which the corresponding electronic edge energy (E_g) of LMCT transitions can be estimated.[60] UV-Vis diffuse-reflectance spectra (DRS) show that the synthesized UiO-68-NH_2 (*ca.* 2.67 eV) and UiO-68-Fe-bpy (*ca.* 1.87 eV) have a similar absorption band in the region of 250–380 nm (Fig. S14 and S15, ESI†), which can be ascribed to the absorption of the Zr–O cluster.[61] However, UiO-68-Fe-bpy exhibits an extra absorption band with the edge extending to around 700 nm in the visible light region, in agreement with the dark red color. These results suggest that UiO-68-Fe-bpy exhibits a better absorption capacity of visible light after the PSM.

The electrochemical properties of TPDC-Fe-bpy were investigated by cyclic voltammetry (Fig. S16, ESI†) in a 0.1 M *n*-Bu_4NPF_6/DMF supporting electrolyte saturated with CO_2. When the electrochemical potential is scanned in the reductive direction, three distinct redox waves at −0.012 (process 1), −0.626 (process 2) and −0.971 (process 3) V *versus* SCE were observed, which can be attributed to Fe(III/II), Fe(II/I) and Fe(I/0).[62] As shown in Fig. S17, ESI,† compared to a N_2 atmosphere, the redox couple Fe(II/I) becomes irreversible, which suggests that Fe(I) can have interaction with CO_2 (Scheme S1†). The excited state potential (E^*) of UiO-68-Fe-bpy was estimated using the equation, $E^* = E_{(FeII/I)} + E_g$, where $E_{(FeII/I)}$ is the ground state potential and E_g is the above-mentioned electronic edge energy. E^* was calculated to be about 1.24 V, implying that the electrons can be transferred from UiO-68-Fe-bpy to CO_2.[63] The results together suggest that UiO-68-Fe-bpy has the appropriate energetics and redox properties to catalyze the photocatalytic reduction of CO_2 to form CO.

Photochemical CO_2 conversion experiments

With the successful modification of Fe(bpy)Cl_3 into the robust MOF UiO-68-NH_2 and its feasibility as a photocatalyst for CO_2 reduction, we evaluated the activity and selectivity of UiO-68-Fe-bpy for photocatalytic CO_2 reduction in the presence of TEOA as an electron donor upon visible light irradiation. As shown in Fig. S18, ESI,† the FID, which monitors CO and CH_4, showed that CO was detected with a retention time of about 1.290 min while no CH_4 (retention time: 2.540 min) was detected. On the other hand, the TCD, which monitors H_2 generation, showed that no H_2 (retention time: 0.578 min) was detected. Besides, the ^{1}H-NMR spectrum was used to detect the liquid product of the photocatalytic reaction and the results show that no liquid product is produced in the reaction system (Fig. S19, ESI†). These results together suggest that the selectivity of CO_2 photoreduction to CO is 100%. Such high selectivity may be due to the solvent-free photocatalytic reaction system as reported previously,[64] in which TEOA acts as electron and proton donors and is oxidized to 2-(bis(2-hydroxyethyl)amino)acetaldehyde.[65] As shown in Fig. 3a, the control experiment with the Xe lamp off shows that CO_2 to CO did not occur, suggesting that this reaction is light-driven. When the

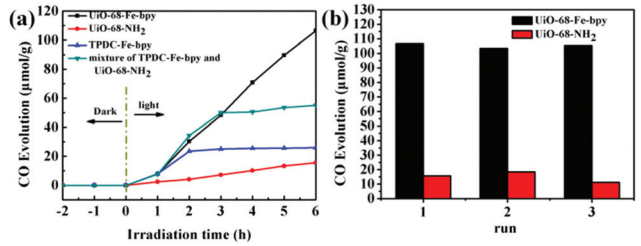

Fig. 3 (a) Photocatalytic CO evolution of UiO-68-NH_2, TPDC-Fe-bpy and UiO-68-Fe-bpy (2 mg photocatalyst). (b) Recycling performance of UiO-68-NH_2 and UiO-68-Fe-bpy.

system was operated in the presence of UiO-68-NH_2 under visible-light illumination, CO_2 was split into CO at a reaction evolution of 10.01 μmol g^{-1} for six hours. Compared to the poor activity of UiO-68-NH_2, UiO-68-Fe-bpy exhibits much better photocatalytic efficiency (about 10 times that of UiO-68-NH_2, Fig. 3a), suggesting that the incorporated Fe(bpy)Cl_3 plays a critical role in improving its photocatalytic activity. It is noteworthy that the photocatalytic efficiency of UiO-68-Fe-bpy is better than those of some typical MOFs and inorganic materials (Table S3, ESI†). Moreover, the photocatalytic performance of the physical mixture of TPDC-Fe-bpy and UiO-68-NH_2 was evaluated under the same catalytic conditions. As shown in Fig. 3a, the system stopped generating CO after three hours upon visible-light illumination, while UiO-68-Fe-bpy can steadily generate CO for at least 6 hours, suggesting that UiO-68-NH_2 can improve the stability of Fe(bpy)Cl_3, and the CO_2 reduction activity of UiO-68-Fe-bpy is not a simple sum of Fe-bpy and UiO-68-NH_2 activities. The covalent linkage of C═N between UiO-68-NH_2 and bpy could provide the ideal stability of UiO-68-Fe-bpy after the PSM, which can prevent the Fe complex from decomposing under visible light illumination.[66] A proposed mechanism for photocatalytic CO_2 reduction over the UiO-68-Fe-bpy under visible light is shown in Scheme S1.† Furthermore, the recycling experiments show that a negligible change was observed in the CO-production yield during the three runs for 18 h (Fig. 3b). PXRD patterns (Fig. S20, ESI†) and SEM results (Fig. S21, ESI†) confirm that the crystallinity and structural integrity were retained after the photocatalytic reactions, suggesting that irradiation does not lead to the photodegradation of the catalyst within 18 hours. The results of each cycle obtained by ICP are shown in Table S4, ESI.†

Femtosecond transient absorption (TA) spectroscopy characterization

While the capability of UiO-68-Fe-bpy MOFs as efficient photocatalysts for CO_2 reduction has been successfully demonstrated by the above photocatalytic experiments, it is necessary to study the excited state (ES) dynamics in order to figure out the specific roles that MOFs play in catalytic reactions. Femtosecond TA spectroscopy was used to investigate the ES dynamics of UiO-68-Fe-bpy MOFs. Fig. 4a and b shows the TA spectra of TPDC-Fe-bpy on an Al_2O_3 film and UiO-68-Fe-bpy MOFs following 400 nm excitation, respectively. The Al_2O_3 film was used as a control to illustrate the intrinsic effect of the porous surface on ES dynamics. As shown in Fig. 4a, the spectrum of TPDC-Fe-bpy exhibits a negative band centered at 570 nm, which can be assigned to the ground state bleach (GSB). At an early time period (<2 ps), two positive features identified as ES absorption were observed at 460–500 nm and 650–800 nm regions. The ES signal at 460–500 nm was quickly replaced by a negative feature, which can be attributed to the overlap of ES absorption with GSB and the faster decay of ES than the GSB recovery. Compared to TPDC-Fe-bpy, UiO-68-Fe-bpy shows similar GSB centered at 600 nm, which is consistent with the UV-Vis ground state absorption spectrum. However, distinct differences were observed between the GSB recovery kinetics of two samples. As shown in Fig. 4c, the recovery of GSB in UiO-68-Fe-bpy is slower than TPDC-Fe-bpy on the Al_2O_3 film, which suggests that the recovery of ES molecules to the ground state was inhibited in UiO-68-Fe-bpy and thus a longer lived ES of the Fe complex in UiO-68-Fe-bpy. One possible explanation for the elongated ES lifetime is that the rigid framework plays an important role in stabilizing the charged separated excited state and suppressing the undesired charge recombination, which has also been observed in previously published work.[67] Therefore, the prolonged ES lifetime of a photocatalyst is beneficial for charge transfer from the sacrificial donor to the catalyst or from the catalyst to reduce CO_2,

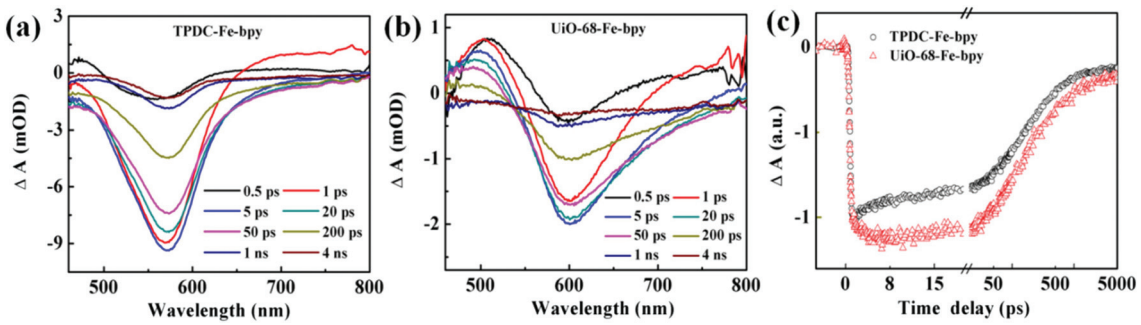

Fig. 4 Femtosecond TA spectra of (a) TPDC-Fe-bpy and (b) UiO-68-Fe-bpy. (c) Comparisons of the ground state bleach (GSB) recovery between TPDC-Fe-bpy and UiO-68-Fe-bpy.

which well explains the enhanced catalytic performance of UiO-68-Fe-bpy with respect to TPDC-Fe-bpy for CO_2 reduction.

Conclusions

In summary, we have successfully synthesized a MOF photocatalyst by incorporating Fe(bpy)Cl_3 using PSM, which shows an enhanced light-absorbing ability and undergoes highly efficient CO_2 reduction to form CO with 100% selectivity under visible-light irradiation. Using transient absorption spectroscopy, we show that Fe(bpy)Cl_3 in UiO-68-NH_2 has longer-lived ES and slower recovery of GSB, which is beneficial for boosting the efficiency of photocatalytic CO production. In addition, the robust nature of UiO-68 ensured the stability of the photocatalyst (UiO-68-Fe-bpy), enabling at least three cycles (18 h) of the photocatalytic process. This work not only reports a new MOF photocatalyst for CO_2 reduction with perfect selectivity for CO generation but also elucidates that PSM is an effective strategy to introduce molecular metal complexes for the optimization of MOF-based materials for photocatalysis.

Conflicts of interest

There are no conflicts to declare.

Acknowledgements

We gratefully acknowledge the National Basic Research Program of China (grant no. 2017YFA0303504) for financial support of this work. This work was also supported by a Project Funded by the Priority Academic Program Development of Jiangsu Higher Education Institutions. The use of the Advanced Photon Source at Argonne National Laboratory was supported by the U. S. Department of Energy, Office of Science, Office of Basic Energy Sciences, under Award No. DE-AC02-06CH11357. S. Y. acknowledges the John J. Eisch fellowship during the 2018–2019 academic year.

Notes and references

1 J. Artz, T. E. Muller, K. Thenert, J. Kleinekorte, R. Meys and W. Leitner, *Chem. Rev.*, 2018, **118**, 434–504.
2 J. Di, C. Zhu, M. Ji, M. Duan, R. Long, C. Yan, K. Gu, J. Xiong, Y. She, J. Xia, H. Li and Z. Liu, *Angew. Chem., Int. Ed.*, 2018, **57**, 14847–14851.
3 C. Hu, X. Hu, R. Li and Y. Xing, *J. Hazard. Mater.*, 2020, **385**, 121599–121603.
4 T. Kajiwara, M. Fujii, M. Tsujimoto, K. Kobayashi, M. Higuchi, K. Tanaka and S. Kitagawa, *Angew. Chem., Int. Ed.*, 2016, **55**, 2697–2700.
5 R. Heng, S. Lucianac, B. Julien and R. Marc, *Nature*, 2017, **548**, 74–77.
6 Y. Huang, Z. Guo, H. Liu, S. Zhang, P. Wang, J. Lu and Y. Tong, *Adv. Funct. Mater.*, 2019, **29**, 1903490–1903499.
7 M. Matsuoka and M. Anpo, *J. Photochem. Photobiol., C*, 2003, **3**, 225–252.
8 W. Lin and H. Frei, *J. Am. Chem. Soc.*, 2005, **127**, 1610–1611.
9 S. Habisreutinger, L. Schmidt-Mende and J. Stolarczyk, *Angew. Chem., Int. Ed.*, 2013, **52**, 7372–7408.
10 Y. Tamaki, T. Morimoto, K. Koike and O. Ishitani, *Proc. Natl. Acad. Sci. U. S. A.*, 2012, **109**, 15673–15678.
11 S. Sato, T. Morikawa, T. Kajino and O. Ishitani, *Angew. Chem., Int. Ed.*, 2013, **52**, 988–992.
12 V. Sara, N. Kornienko, C. Margarit, P. Yang and C. Chang, *J. Am. Chem. Soc.*, 2013, **135**, 14413–14424.
13 A. Morris, G. Meyer and E. Fujita, *Acc. Chem. Res.*, 2009, **42**, 1983–1994.
14 Y. Qu and X. Duan, *Chem. Soc. Rev.*, 2013, **42**, 2568–2580.
15 A. McKinlay, R. Morris, P. Horcajada, G. Ferey, R. Gref, P. Couvreur and C. Serre, *Angew. Chem., Int. Ed.*, 2010, **49**, 6260–6266.
16 K. Taylor-Pashow, J. DellaRocca, Z. Xie, S. Tran and W. Lin, *J. Am. Chem. Soc.*, 2009, **131**, 14261–14263.
17 L. Murray, M. Dinca and J. Long, *Chem. Soc. Rev.*, 2009, **38**, 1294–1314.
18 J. Rowsell and O. Yaghi, *Angew. Chem., Int. Ed.*, 2005, **44**, 4670–4679.
19 R. Matsuda, R. Kitaura, S. Kitagawa, Y. Kubota, R. Belosludov, T. Kobayashi, H. Sakamoto, T. Chiba, M. Takata, Y. Kawazoe and Y. Mita, *Nature*, 2005, **436**, 238–241.
20 J. Lang, Q. Xu, R. B. Yuan and B. F. Abrahams, *Angew. Chem., Int. Ed.*, 2004, **43**, 4741–4745.
21 D. Liu, J. Lang and B. Abrahams, *J. Am. Chem. Soc.*, 2011, **133**, 11042–11045.
22 L. Bastin, P. Brcia, E. Hurtado, J. Silva, A. Rodrigues and B. Chen, *J. Phys. Chem. C*, 2008, **112**, 1575–1581.
23 Y. Shi, W. Zhang, B. Abrahams, P. Braunstein and J. Lang, *Angew. Chem., Int. Ed.*, 2019, **58**, 9453–9458.
24 F. Li, Q. Shao, X. Huang and J. Lang, *Angew. Chem., Int. Ed.*, 2018, **57**, 1888–1892.
25 F. Li, P. Wang, X. Huang, D. Young, H. Wang, P. Braunstein and J. Lang, *Angew. Chem., Int. Ed.*, 2019, **58**, 7051–7056.
26 F. Hu, Y. Mi, C. Zhu, B. Abrahams, P. Braunstein and J. Lang, *Angew. Chem., Int. Ed.*, 2018, **57**, 12696–12701.
27 A. Corma, H. Garcia and F. Xamena, *Chem. Rev.*, 2010, **110**, 4606–4655.
28 J. Lee, O. Farha, J. Roberts, K. Scheidt, S. Nguyen; and J. Hupp, *Chem. Soc. Rev.*, 2009, **38**, 1450–1459.
29 Y. Fu, D. Sun, Y. Chen, R. Huang, Z. Ding, X. Fu and Z. Li, *Angew. Chem., Int. Ed.*, 2012, **51**, 3364–3367.
30 Y. Chen, D. Wang, X. Deng and Z. Li, *Catal. Sci. Technol.*, 2017, **7**, 4893–4904.
31 D. Wang, R. Huang, W. Liu, D. Sun and Z. Li, *ACS Catal.*, 2014, **4**, 4254–4260.
32 C. Wang, Z. Xie, K. EdeKrafft and W. Lin, *J. Am. Chem. Soc.*, 2011, **133**, 13445–13454.

33 T. Toyao, M. Saito, S. Dohshi, K. Mochizuki, M. Iwata, H. Higashimura, Y. Horiuchi and M. Matsuoka, *Chem. Commun.*, 2014, **50**, 6779–6781.
34 Y. Lin, C. Kong, Q. Zhang and L. Chen, *Adv. Energy Mater.*, 2017, **7**, 1601296.
35 E. Sanz-Perez, C. Murdock, S. Didas and C. Jones, *Chem. Rev.*, 2016, **116**, 11840–11876.
36 J. Liu, P. Thallapally, B. McGrail and D. Brown, *Chem. Soc. Rev.*, 2012, **41**, 2308–2322.
37 Y. Bae and R. Snurr, *Angew. Chem., Int. Ed.*, 2011, **50**, 11586–11596.
38 X. Deng, Y. Qin, M. Hao and Z. Li, *Inorg. Chem.*, 2019, **58**, 16574–16580.
39 D. Sun, Y. Gao, J. Fu, X. Zeng, Z. Chen and Z. Li, *Chem. Commun.*, 2015, **51**, 2645–2648.
40 X. Deng, J. Albero, L. Xu, H. García and Z. Li, *Inorg. Chem.*, 2018, **57**, 8276–8286.
41 C. Cohen, T. Chu and G. Coates, *J. Am. Chem. Soc.*, 2005, **127**, 10869–10878.
42 J. Louie, J. Gibby, M. Farnworth and T. Tekavec, *J. Am. Chem. Soc.*, 2002, **124**, 15188–15189.
43 S. Xie, Q. Zhang, G. Liu and Y. Wang, *Chem. Commun.*, 2016, **52**, 35–59.
44 S. K. Lee, M. Kondo, M. Okamura, T. Enomoto, G. Nakamura and S. Masaoka, *J. Am. Chem. Soc.*, 2018, **140**, 16899–16903.
45 R. Reithmeier, S. Meister, A. Siebel and B. Rieger, *Dalton Trans.*, 2015, **44**, 6466–6472.
46 C. Cometto, R. Kuriki, L. Chen, K. Maeda, T. Lau, O. Ishitani and M. Robert, *J. Am. Chem. Soc.*, 2018, **140**, 7437–7440.
47 H. Takeda, H. Koizumi, K. Okamoto and O. Ishitani, *Chem. Commun.*, 2014, **50**, 1491–1493.
48 V. Sara, N. Kornienko, C. Margarit, P. Yang and C. Chang, *J. Am. Chem. Soc.*, 2013, **135**, 14413–14424.
49 X. Gao, B. Guo, C. Guo, Q. Meng, J. Liang and J. Liu, *ACS Appl. Mater. Interfaces*, 2020, **12**, 24059–24065.
50 W. Liao, J. Zhang, Z. Wang, S. Yin, M. Pan, H. Wang and C. Su, *J. Mater. Chem. A*, 2018, **6**, 11337–11345.
51 H. Rao, L. Schmidt, J. Bonin and M. Robert, *Nature*, 2017, **548**, 74–77.
52 P. Alsabeh, A. Hernández, E. Barsch, H. Junge, R. Ludwig and M. Beller, *Catal. Sci. Technol.*, 2016, **6**, 3623–3630.
53 A. Schaate, P. Roy, A. Godt, J. Lippke, F. Waltz, M. Wiebcke and P. Behrens, *Chem. – Eur. J.*, 2011, **17**, 6643–6651.
54 Y. P. Wei, Y. Liu, F. Guo, X. Y. Dao; and W. Y. Sun, *Dalton Trans.*, 2019, **48**, 8221–8226.
55 J. Wang, M. Yang, W. Dong, Z. Jin, J. Tang, S. Fan, Y. Lu and G. Wang, *Catal. Sci. Technol.*, 2016, **6**, 161–168.
56 L. Garzon, R. Hermida, I. Imaz and D. Maspoch, *J. Am. Chem. Soc.*, 2017, **139**, 897–903.
57 C. Bressler, C. Milne, V. Pham, A. ElNahhas, C. Borca, G. Ingold, R. Abela and M. Chergui, *Science*, 2009, **323**, 489–492.
58 V. Briois, P. Sainctavit, G. Long and F. Grandjean, *Inorg. Chem.*, 2001, **40**, 912–918.
59 H. Fei, M. Sampson, L. Yeob, P. Kubiak and M. Cohen, *Inorg. Chem.*, 2015, **54**, 6821–6828.
60 E. Ross-Medgaarden and I. Wachs, *J. Phys. Chem. C*, 2007, **111**, 15089–15099.
61 D. Sun, Y. Fu, W. Liu, L. Ye, D. Wang and Z. Li, *Chem. – Eur. J.*, 2013, **19**, 14279–14285.
62 C. Cardona, W. Li, A. Kaifer, D. Stockdale and G. Bazan, *Adv. Mater.*, 2011, **23**, 2367–2371.
63 R. Rodrigues, C. Boudreaux, E. Papish and J. Delcamp, *ACS Appl. Energy Mater.*, 2019, **2**, 37–46.
64 X. Y. Dao, J. H. Guo, Y. P. Wei, F. Guo, Y. Liu and W. Y. Sun, *Inorg. Chem.*, 2019, **58**, 8517–8524.
65 S. Q. Wang, X. Y. Zhang, X. Y. Dao, X. M. Cheng and W. Y. Sun, *ACS Appl. Nano Mater.*, 2020, **3**, 10437–10445.
66 W. Wang and T. B. Rauchfuss, *J. Am. Chem. Soc.*, 2012, **134**, 4525–4528.
67 L. Hanna, P. Kucheryavy, C. Liu, X. Zhang and J. Lockard, *J. Phys. Chem. C*, 2017, **121**, 13570–13576.